Smart Structures and Systems, *Vol. 22, No. 2 (2018) 201-207*
DOI: https://doi.org/10.12989/sss.2018.22.2.201

Multiple crack evaluation on concrete using a line laser thermography scanning system

Keunyoung Jang and Yun-Kyu An*

Department of Architectural Engineering, Sejong University,
209 Neungdong-ro, Gwangjin-gu, Seoul 05006, Republic of Korea

(Received May 20, 2017, Revised November 18, 2017, Accepted November 28, 2017)

Abstract. This paper proposes a line laser thermography scanning (LLTS) system for multiple crack evaluation on a concrete structure, as the core technology for unmanned aerial vehicle-mounted crack inspection. The LLTS system consists of a line shape continuous-wave laser source, an infrared (IR) camera, a control computer and a scanning jig. The line laser generates thermal waves on a target concrete structure, and the IR camera simultaneously measures the corresponding thermal responses. By spatially scanning the LLTS system along a target concrete structure, multiple cracks even in a large scale concrete structure can be effectively visualized and evaluated. Since raw IR data obtained by scanning the LLTS system, however, includes timely- and spatially-varying IR images due to the limited field of view (FOV) of the LLTS system, a novel time-spatial-integrated (TSI) coordinate transform algorithm is developed for precise crack evaluation in a static condition. The proposed system has the following technical advantages: (1) the thermal wave propagation is effectively induced on a concrete structure with low thermal conductivity of approximately 0.8 W/m K; (2) the limited FOV issues can be solved by the TSI coordinate transform; and (3) multiple cracks are able to be visualized and evaluated by normalizing the responses based on phase mapping and spatial derivative processes. The proposed LLTS system is experimentally validated using a concrete specimen with various cracks. The experimental results reveal that the LLTS system successfully visualizes and evaluates multiple cracks without false alarms.

Keywords: concrete crack evaluation; IR thermography; line laser scanning; time-spatial-integrated coordinate transform; phase mapping process; nondestructive test

1. Introduction

Concrete is one of the most widely used construction materials, accounting for around 60% of civil infrastructures in Korea (KMS 2017). Although concrete structures have high compressive strengths, they are typically susceptible to tensile stresses. Thus, cracks are often inevitably produced in concrete structures. These concrete cracks can be inherently generated by shrinkage during the curing process, but most severe structural-level cracks are generated by external loads. Once the structural-level cracks occur in concrete structures, they may propagate along the surface and through-the-thickness directions by repeated external loads. Such crack propagation may cause serious problems such as strength reduction, corrosion of reinforcing rebar and even structural failure. Therefore, concrete cracks should be detected and managed from their early stage. During the last few decades, visual inspection performed by experts has been widely used in the fields. However, the visual inspection is often unreliable, labor-intensive and sometimes not applicable to inaccessible areas of a target structure (Chang *et al*. 2003).

To tackle the aforementioned issues, a number of nondestructive evaluation (NDE) techniques have been proposed. Ultrasonic techniques have high accuracy and sensitivity for crack evaluation as a contact-type NDE technique (Tawie *et al*. 2010, Hall and Popovics 2016, Zhang *et al*. 2017, Lee *et al*. 2017). However, ultrasonic waves inherently have high attenuation rate in concrete materials, making it difficult to inspect large area using a few ultrasonic sensors. Thus, many sensors are often required for large area inspection. Moreover, complex signal interpretation is typically required due to the inhomogeneous characteristics of concrete. As another contact-type NDE technique, fiber reinforced concrete techniques have been proposed (Chen *et al*. 1993, Han *et al* 2012). By inserting conductive fibers into concrete materials, a concrete structure is able to be used as a sensor itself. However, they also require a number of spatial measurement points to cover the large inspection area. Moreover, their crack detection performance highly depends on the manufacturing process, and environmental effects such as temperature and humidity variations on the performance are not fully validated yet.

To overcome the limitations of the contact-type NDE techniques, noncontact NDE techniques have been proposed. One of the most widely accepted noncontact NDE techniques is a vision image-based crack detection technique. The vision technique is simple, noncontact, cost-effective and capable of autonomous crack detection (Jahanshahi and Masri. 2013, Koch *et al*. 2014, Liu *et al*. 2014, Kim *et al*. 2017). Thanks to these advantages, the vision technique combining with unmanned aerial vehicles

---

∗Corresponding author, Professor
E-mail: yunkyuan@sejong.ac.kr

http://www.techno-press.com/journals/sss&subpage=7

ISSN: 1738-1584 (Print), 1738-1991 (Online)

(UAVs) has been recently proposed. Eschmann *et al.* tried to detect cracks of building using vision images obtained by UAVs (Eschmann *et al*. 2012). Then, Kim *et al.* proposed a crack detection system using static vision images captured by a vision camera embedded on UAVs (Kim *et al*. 2015). Similarly, Hennriques and Roque inspected cracks of concrete dam using UAVs-captured images (Hennriques and Roque 2015). However, the performance of the vision technique highly depends on the image capturing conditions such as capturing angle, illuminance and undesired dust in the air or target surface. Moreover, since a vision camera typically has a limited field of view (FOV), large area inspection may not be effective.

Alternatively, infrared (IR) thermography techniques have been used for concrete crack detection. Sham *et al.* evaluated concrete cracks using flash IR thermography (Sham *et al*. 2008), and Zenzinger *et al*. tried to detect cracks using eddy current IR thermography (Zenzinger *et al*. 2007). The IR thermography has high crack detectability and robustness against surrounding noises such as illuminance, dust and so on. However, large inspection area cannot be effectively covered using the conventional IR techniques, because optical lamps and eddy current used as heat sources for thermal wave generation have the limited working distance. Moreover, an IR camera also encounters the limited FOV issues. More recently, An *et al*. and Yang *et al*. proposed laser IR thermography techniques adapting various laser beam shapes as the heat sources for crack detection (An *et al*. 2014, An *et al*. 2015, Yang *et al*. 2016). Although the use of laser enables to extend the working distance and to precisely control thermal wave generation, the limited FOV issue could not be solved. Note that large FOV has the low pixel resolution, while small FOV has high pixel resolution. Furthermore, multiple crack visualization is not achieved in a single image, because macro-crack-induced features are more dominant than the micro-crack ones.

In this study, a line laser thermography scanning (LLTS) system is proposed to overcome the aforementioned technical hurdles. The basic premise is that line laser thermography system is developed as the core technology for the upcoming UAV-mounted crack inspection. The LLTS system basically utilizes a continuous-wave (CW) line laser source for thermal wave generation, an IR camera for measuring the corresponding thermal responses, and a scanning jig for moving the LLTS system along the predetermined scanning route. The LLTS system has the following technical superiorities: (1) fully noncontact, nondestructive and fast crack evaluation can be achieved especially on large concrete structures; (2) the limited FOV issue can be tackled by developing a time-spatial-integrated (TSI) coordinate transform algorithm, making it possible to precisely evaluate cracks on the entire region of interest (ROI) in a static condition; (3) multiple cracks are effectively visualized and evaluated by normalizing the responses based on phase mapping and spatial derivative processes; (4) false alarms caused by environmental and inspection conditions can be minimized; and (5) making decision for crack evaluation can be instantaneously performed without accumulated baseline data.

This paper is organized as follows. Section 2 describes the development of the LLTS system. Then, a multiple crack evaluation algorithm including the TSI coordinate transform, phase mapping and spatial derivative processes is developed in Section 3. Section 4 shows the experimental validation using a lab-scale concrete specimen with various-size cracks. Finally, the paper concludes with a brief summary and discussion in Section 5.

2. Development of the line laser thermography scanning (LLTS) system

Fig. 1 shows the LLTS system composed of excitation, sensing and control units. The excitation unit consists of the CW laser and line beam generator, generating thermal waves onto the target concrete structure. Then, the sensing unit is comprised of the IR camera to measure the corresponding thermal wave propagation along the concrete structure. The control computer in the control unit contains the control and processing programs coded by LABVIEW® and MATLAB®, respectively. The LLTS system is mounted on a scanning jig for moving along the predetermined scanning route as shown in Fig. 1. Here, the excitation unit, sensing unit and scanning jig are all synchronized and controlled by the control computer.

The working principle of the LLTS system is as follows. Once the control computer in the control unit sends out control signals to the excitation unit, sensing unit and scanning jig, the laser driver generates a current signal to activate the CW laser emitting a point laser beam. The point laser beam is transformed to a line-shape laser beam through the line beam generator in the excitation unit. Simultaneously, the IR camera in the sensing unit is operated to acquire the thermal wave responses. When the control signal is transmitted to the scanning jig from the control computer, the LLTS system automatically scans the target structure along the predetermined scanning route. Then, the thermal waves are generated, and the corresponding thermal responses are acquired under changing the time and spatial domains. The measured thermal images are instantaneously transmitted to and saved in the control computer as raw IR (I^R) images. The I^R images need to be processed for precise crack evaluation because they timely and spatially vary. Note that the LLTS system will be mounted onto UAVs instead of the scanning jig for practical useages although its miniaturization and optimization are still underway.

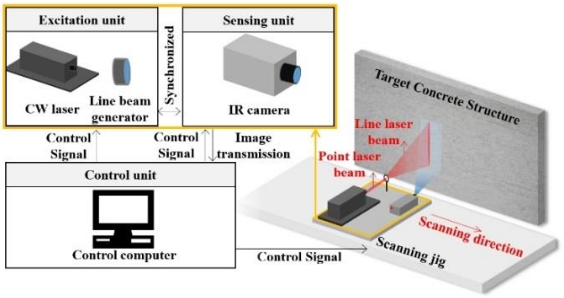

Fig. 1 Schematics of the proposed LLTS system

3. Development of the multiple crack evaluation algorithm

This section explains how multiple concrete cracks are precisely evaluated from the I^R images. Since the I^R images acquired by scanning the LLTS system are continuously changed in the time and spatial domains, precise crack evaluation is difficult in the practical point of view. Thus, the spatially scanned I^R images as a function of time need to be eventually converted to the spatially-integrated and processed. Fig. 2 shows the overview of the multiple crack evaluation algorithm consisted of the following three steps: (1) image distortion calibration, (2) TSI coordinate transform and (3) phase mapping and spatial derivative.

3.1 Image distortion calibration

Since the I^R images are often distorted due to the wide angles of the camera lens, distortion calibration is needed for precise crack evaluation. In this study, the camera calibration algorithm developed by Zhang. for vision images is used (Zhang 2010), because the IR camera can also be assumed as a pin-hole vision camera model (Vidas *et al*. 2012)

$$s\begin{bmatrix} x \\ y \\ z \\ 1 \end{bmatrix} = A[R|t]\begin{bmatrix} X \\ Y \\ Z \\ 1 \end{bmatrix} \tag{1}$$

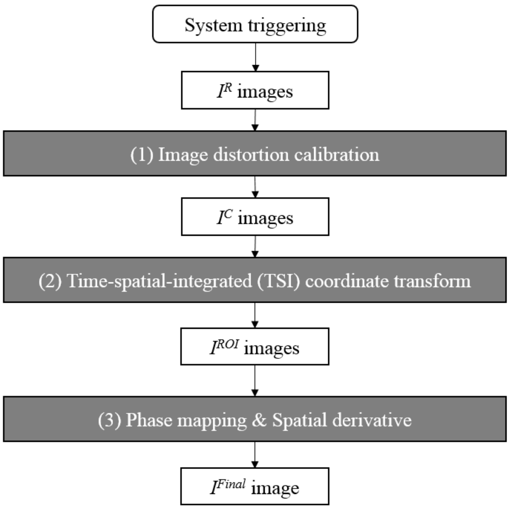

Fig. 2 Overview of the proposed crack evaluation algorithm: I^R, I^C, I^{ROI} and I^{Final} are the raw, calibrated, TSI transformed and final IR images, respectively.

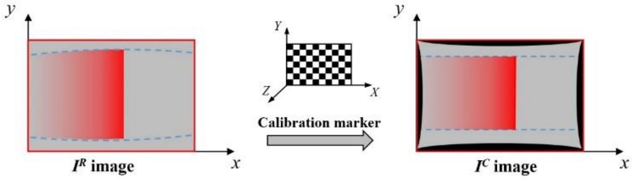

Fig. 3 Image distortion calibration using a calibration marker

where s is an arbitrary scale factor. $[x\ y\ z\ 1]^{\mathrm{T}}$ and $[X\ Y\ Z\ 1]^{\mathrm{T}}$ represent the camera and world coordinates, respectively. A and $[R|t]$ are the IR camera's intrinsic and extrinsic parameters. In particular, R and t is the rotation and translation matrices. The pin-hole camera model describes the mathematical relationship between the 3D real world coordinate and the projection on the 2D image plane. The calibration marker represents 3D real world coordinate. Without loss generality, the calibration marker is assumed on Z=0. Then, a homography matrix (H) between the calibration marker and the IR image is defined as

$$H = [h_1\ h_2\ h_3] = \lambda A[r_1\ r_2\ t] \tag{2}$$

where λ is an arbitrary scalar. r_1 and r_2 denote the elements of R. Given an image of the calibration marker, H can be estimated based on maximum likelihood criterion. Using the fact that r_1 and r_2 are orthonormal, it gives (Kanatani *et al*. 2000)

$$h_1^{\mathrm{T}} A^{-\mathrm{T}} A^{-1} h_2 = 0 \tag{3}$$

$$h_1^T A^{-T} A^{-1} h_1 = h_2^T A^{-T} A^{-1} h_2 \tag{4}$$

Each homography provides the two basic constraints on the camera intrinsic. Three independent orientations are sufficient to solve for camera intrinsic linearly. If A is known by closed-form solution (Brown. 1971), the extrinsic parameters can be readily obtained.

$$\begin{aligned} r_1 &= \lambda A^{-1} h_1, \\ r_2 &= \lambda A^{-1} h_2, \\ t &= \lambda A^{-1} h_3 \end{aligned} \tag{5}$$

Once the intrinsic and extrinsic parameters of the IR camera are obtained using the calibration marker, the I^C images can be obtained from the I^R images using Eq. (1).

3.2 Time-spatial-integrated (TSI) coordinate transform

Because the LLTS system continuously moves along the predetermined scanning route, the physical inspection area in the I^C images is also continuously changed as a function of time. Thus, it is difficult to analyze thermal wave propagation on the entire ROI using the I^C images. In this step, the I^C image is transformed to the spatially-integrated ROI (I^{ROI}) image using the TSI coordinate transform.

First, the analysis area exposed to the laser excitation needs to be determined within FOV because the line laser excitation may not cover the entire FOV as shown in Fig. 4. Assuming that the LLTS system scans along the x direction in Fig. 4, the intensity profile of the line laser beam typically follows a Gaussian distribution (An *et al*. 2014). Thus, the analysis area can be determined by tracing the mid-points along the x axis and their affected boundaries along the y axis. Here, the mid-points can be selected using $\mu(x)$ of the Gaussian distribution, and the affected boundary is able to be obtained by calculating 95% confidence interval of the Gaussian distribution as shown Fig. 4. Note that the analysis area physically means where the enough thermal energy is injected by the line laser beam to induce thermal wave propagation within the I^C images.

Next, the determined analysis areas are spatially integrated as a function of time using the following TSI coordinate transform, making it possible to reconstruct the I^{ROI} images as described in Fig. 5.

$$\begin{bmatrix} x* \\ y \\ t* \end{bmatrix} = \begin{bmatrix} 0 & 0 & v & 0 \\ 0 & 1 & 0 & -\mu(x) \\ 1/v & 0 & 0 & 0 \end{bmatrix} \begin{bmatrix} x \\ y \\ t \\ 1 \end{bmatrix} \tag{6}$$

where $\mu(x) - 2\sigma \leq y \leq \mu(x) + 2\sigma$. v is the scanning speed. The superscript * means the transformed coordinate. The y axis is constant because only x directional scanning is assumed in this study. The TSI coordinate transform is based on the physical phenomenon that a specific spatial point is heated and subsequently cooled by the line laser exposure as time passed. The x axis data on the I^C images can be regarded as the thermal variation in the time domain at a specific point of FOV, and the t axis data on I^C images is able to be considered as the thermal change in the spatial domain at a specific time. Thus, each data can be converted into the new integrated ROI coordinate, i.e. x*, y and t* axes, using Eq. (6). The I^{ROI} images eventually show as if the entire ROI is simultaneously and uniformly heated and subsequently cooled in the spatially stationary condition.

3.3 Phase mapping and spatial derivative

Since the I^{ROI} images cannot properly reveal multiple cracks, additional data processing called the phase mapping is necessary for precise multiple crack evaluation as shown in Fig. 6. In particular, macro-cracks are typically overwhelmed while micro-cracks are hidden due to the amplitude difference of the crack-induced features.

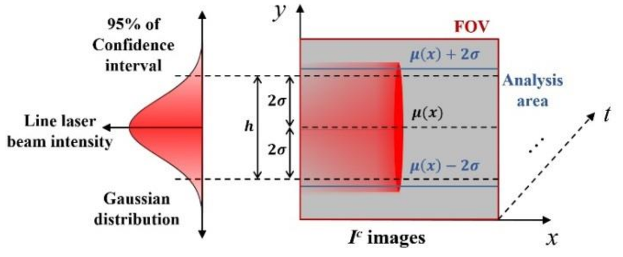

Fig. 4 Determination of the analysis area on the I^C image

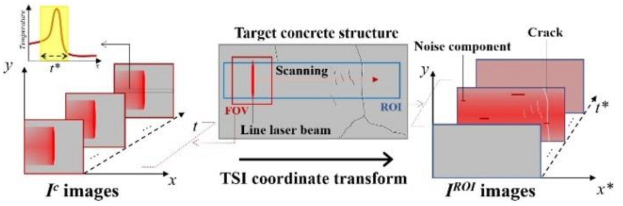

Fig. 5 TSI coordinate transform

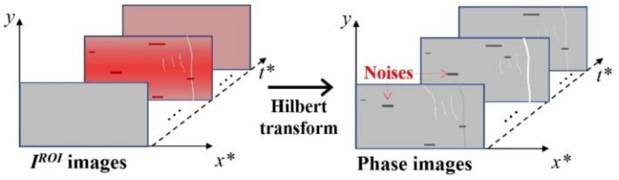

Fig. 6 Phase mapping process using Hilbert transform

The phase mapping process enables various-size cracks to be effectively visualized by normalizing the crack-induced features along all pixels of interest. First, all pixel values of the I^{ROI} images are transformed to the complex values along the t* axis using Hilbert transform (Hahn. 1996).

$$H(x^*, y, t^*) = P\frac{1}{\pi}\int_{-\infty}^{\infty} \frac{I^{ROI}(x^*, y, \tau)}{t^* - \tau} d\tau \tag{7}$$

where P is the Cauchy value of the integral, and τ is the short time interval. Then, the instantaneous phase values of each pixel are simply obtained by calculating the angle between real and imaginary parts of the transformed I^{ROI} images.

$$\theta(x^*, y, t^*) = arctan\left(\frac{Im[H(x^*, y, t^*)]}{Re[H(x^*, y, t^*)]}\right) \tag{8}$$

where Re and Im represent the real and imaginary parts, respectively. $\theta(x^*, y, t^*)$ denotes the phase image. Eq. (8) physically means that the responses are normalized between -π to π, making it possible to effectively visualize even hidden micro-cracks. However, not only crack-induced feature but also undesired noise components might be augmented by the phase mapping process. Thus, the denoising process is subsequently carried out as shown in Fig. 7.

First, $\theta(x^*, y, t^*)$ is accumulated along the t* axis.

$$\emptyset(x^*, y) = \sum_{t^*} \theta(x^*, y, t^*) \tag{9}$$

where $\emptyset(x^*, y)$ is the accumulation image. Then, the spatial derivative is subsequently applied to $\emptyset(x^*, y)$ along the x* direction which is the scanning direction in this study.

$$F(x^*, y) = \frac{\partial \emptyset(x^*, y)}{\partial x^*} \tag{10}$$

where $F(x^*, y)$ is the I^{Final} image. Finally, the I^{Final} image visualizes multiple cracks without noise components in the static conditions covering the entire ROI.

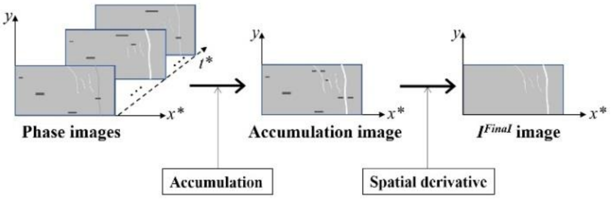

Fig. 7 Denoising process based on spatial derivative

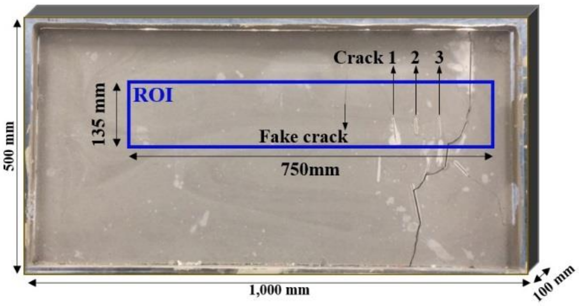

Fig. 8 Specially designed concrete specimen with various-size cracks and ROI used in the test

4. Lab-scale experimental validation

4.1 Experimental setup

The LLTS system is experimentally validated using a lab-scale concrete specimen with multiple cracks as shown in Fig. 8. The specially designed concrete specimen has dimensions of 1000 x 500 x 100 mm^3. The target concrete specimen with 103 MPa compressive strength is prepared by mixing cement, silica sand, fly ash, super-plasticizer and water. The mixing composition is summarized in Table 1. During the curing process, 150 µm-width acrylic slots are inserted to make artificial cracks. The generated artificial cracks are divided into the two types: macro-crack (≥ 500 µm) and micro-crack (< 500 µm), defined in this study for the convenience. In addition, a fake crack with 1mm width is created using a pencil for the positive false alarm test. Then, the size of the target ROI is 750 x135 mm^2 as shown in Fig. 8. The target ROI includes the three different types of real cracks, the fake crack and non-cracked area.

Table 1 Mixing composition of the concrete specimen (%)

Cement (Type)	Silica sand	Fly ash	Super-plasticizer	Water
100 (Ⅲ)	100	15	0.9	35

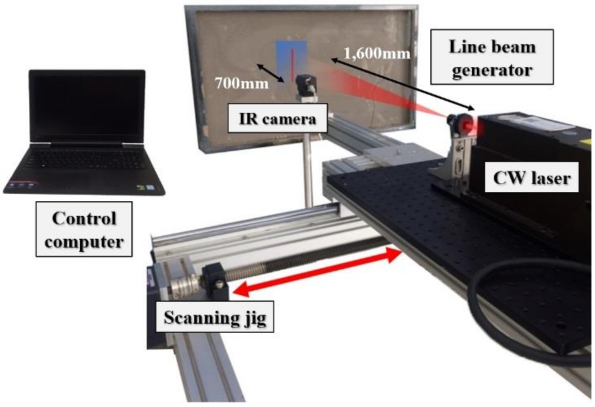

Fig. 9 Experimental setup of the LLTS system

Fig. 9 shows the lab-scale experimental setup of the LLTS system with the concrete specimen. The control computer sends out control signals to the CW laser (TMA-532-15, TMA) generating a point laser beam with a wavelength of 532 nm. Then, the point laser beam is converted to the line laser beam through the line beam generator installed in 1,600 mm apart from the concrete specimen. The size of line laser beam is 1 x135 mm^2, and the line laser beam intensity is set to approximately 111.11 mW/mm^2 in the test. Here, the intensity of the line laser beam needs to be optimized by considering the scanning speed (23 mm/s) and thermal conductivity of the concrete specimen (0.8 W/m K). The corresponding thermal responses are measured using the IR camera (A65, FLIR) with a frame rate of 30Hz, a spectral range of 3 µm to 5 µm, a pixel resolution of 640 x 512. The IR camera is installed 700 mm away from the target specimen, and the corresponding FOV has height, width and spatial resolution of 235 mm, 300 mm, and 476 µm, respectively.

4.2 Experimental results

Once the I^R images are obtained using the LLTS system, the I^C images are obtained by conducting the calibration process using a calibration marker as explained in the subsection 3.1. Fig. 10 shows the representative I^C images obtained by scanning the concrete specimen. As expected, the I^C images within FOV are timely and spatially changed, making it difficult to be analyzed as they are. Then, the $\mu(x)$ and σ values are computed on the I^C images as described in Fig. 4. The determined ROI has a height of 135 mm equivalent to 300 pixels in the I^C images. Subsequently, the I^{ROI} images are constructed using the TSI coordinate transform defined in Eq. (6). Fig. 11 shows the representative I^{ROI} image right after the laser excitation at each spatial point. Even though the line laser is subsequently scanned along ROI, it looks as if the entire ROI is simultaneously and uniformly heated. In reality, the laser heating is not perfectly uniform on ROI, but thermal wave generation is enough to analyse the crack existence within ROI. Although crack existence can be intuitively observed, still there are a number of unwanted noises and disturbances in the I^{ROI} image as displayed in Fig. 11.

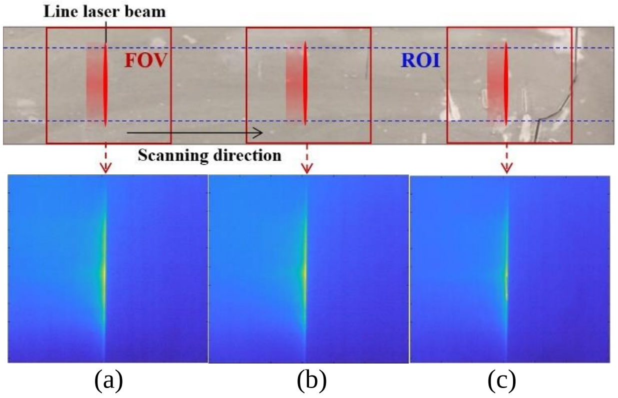

Fig. 10 Representative I^C images after (a) 5 seconds, (b) 15 seconds and (c) 25 seconds

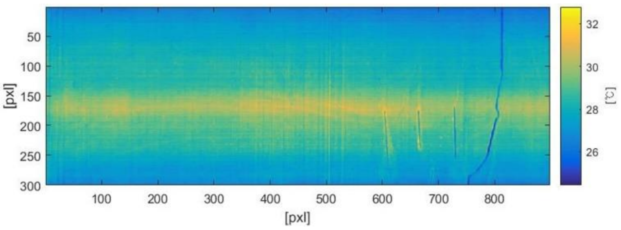

Fig. 11 Representative I^{ROI} image

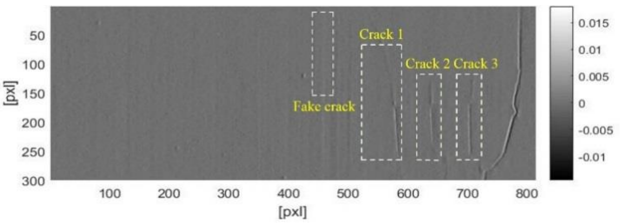

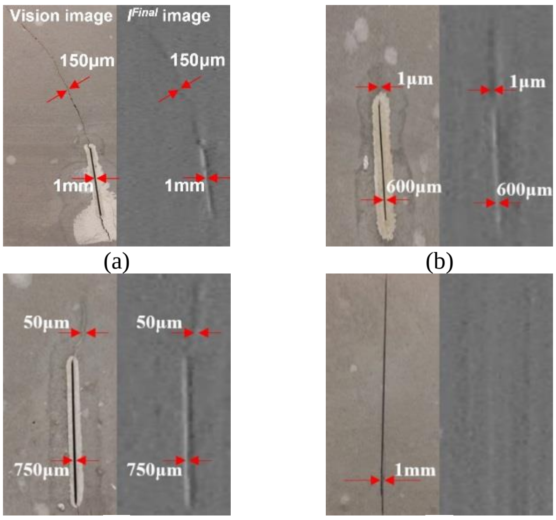

(a) (b)

(c) (d)

Fig. 13 Comparison between the vision I^{Final} images: (a) crack 1, (b) crack 2, (c) crack 3 and (d) fake crack

To precisely evaluate multiple cracks, the phase mapping and spatial derivative processes are subsequently applied to the I^{ROI} images. Fig. 12 reveals that various-size cracks are clearly visualized in the I^{Final} image without undesired noise components. In particular, micro-cracks are well visualized regardless of the amplitude difference even when macro- and micro-cracks coexist in a single image. To more specifically, crack quantification results are compared with the high resolution vision images in Fig. 13. The three different types of crack are enlarged. First, both 1 mm-width macro-crack and 150 μm-width micro-crack are successfully visualized in Fig. 13(a) even they coexist. Then, the almost closed-type micro-cracks having widths from 1 μm to 50 μm are also well detected in Figs. 13(b) and 13(c) even when 1 μm micro-crack is hardly seen in the vision image. One more interesting thing to see in Fig. 13 (d) is that the fake crack artificially made by the pencil is not highlighted, meaning that no positive false alarm is indicated. It can be confirmed that the proposed technique enhances the crack detectability and especially visibility of multiple cracks. Furthermore, positive false alarms caused by surface disturbances can be minimized.

5. Conclusions

This paper proposed a line laser thermography scanning (LLTS) system and the corresponding multiple crack evaluation algorithm as the core technology for unmanned aerial vehicle (UAV)-mounted concrete crack inspection. The LLTS system is able to rapidly and precisely evaluate multiple cracks especially in a large-scale concrete structure. In particular, timely- and spatially-varying images are transformed to stationary images for precise crack evaluation by developing a time-spatial-integrated coordinate transform algorithm. The proposed technique was experimentally validated using a lab-scale concrete specimen with various-size cracks. The test results revealed that macro- and micro-cracks successfully visualized without positive false alarms even when they coexist in a single image. As a follow-up study, the proposed technique is now being combined with the vision image technique for improving reliability. Then, the LLTS system will be miniaturized and optimized to mount it onto UAVs. After optimizing the proposed technique, outdoor tests under varying environmental and operational conditions will be thoroughly carried out, and it will be applied to real civil infrastructures such as bridge, dam and building.

Acknowledgments

The research described in this paper was financially supported by a grant (17SCIP-C116873-02) from Construction Technology Research Program funded by Ministry of Land, infrastructure and Transport of Korea government and Basic Science Research Program of the National Research Foundation of Korea (NRF) funded by the Ministry of Science, ICT & Future Planning (2015R1C1A1A01052625).

References

An, Y.K., Kim, J.M. and Sohn, H. (2014), “Laser lock-in thermography for detection of surface-breaking fatigue cracks on uncoated steel structures”, *NDT & E Int.*, **65**, 54-63.

An, Y.K., Yang, J.Y., Hwang, S.K. and Sohn, H. (2015), “Line laser lock-in thermography for instantaneous imaging of cracks in semiconductor chips”, *Opt. Laser. Eng.*, **73**, 128-136.

Brown, D.C. (1971), “Close-range camera calibration”, *Photogrammetric Engineering*, **37**(8), 855-866.https://doi.org/10.1.1.14.6358

Chang, P.C., Flatau, A. and Liu, S.C. (2003), “Review paper: health monitoring of civil infrastructure”, *Struct. Health Monit.*, **2**(3), 257–267. https://doi.org/10.1177/1475921703036169

Chen, P.W. and Cheung, D.D.L. (1993), “Carbon fiber reinforced concrete for smart structures capable of non-destructive flaw detection", *Smart Mater. Struct.*, **2**, 22-30.

Eschmann, C., Kuo, C.M. and Boller, C. (2012), "Unmanned aircraft systems for remote building inspection and monitoring", *Proceedings of the 6th European Workshop on Structural Health Monitoring*, Dresden, Germany, July.

FMS (2017), http://www.fms.or.kr

Han, B., Zhang, K., Yu, X., Kwon, E. and Ou, J. (2012), "Electrical characteristics and pressure-sensitive response measurements of carboxyl MWNT/cement composites", *Cement Concrete Compos.*, **34**(6), 794-800. https://doi.org/10.1016/j.cemconcomp.2012.02.012

Hennriques, M.J. and Roque, D. (2015), "Unmanned Aerial Vehicles (UAV) as a support to visual Inspections of concrete dams", *Proceedings of the 2nd International Dam World Conference*, Lisbon, Portugal, April.

Hahn, S.L. (1996), *Hilbert Transforms in Signal Processing*, Artech House, Norwood, United States.

Hall, K.S. and Popovics, J.S. (2016), "Air-coupled ultrasonic tomography of solids: 2 Application to concrete elements", *Smart Struct. Syst.*, **17**(1), 31-43. http://dx.doi.org/10.12989/sss.2016.17.1.031

Jahanshahi, M.R., Masri, S.F., Padgett, C.W. and Sukhatme, G.S. (2013), "An innovative methodology for detection and quantification of cracks through incorporation of depth perception", *Mach. Vision Appl.*, **24**(2), 227–241. https://doi.org/10.1007/s00138-011-0394-0

Koch, C., Paal, S., Rashidi, A., Zhu, Z., König, M. and Brilakis, I. (2014), "Achievements and challenges in machine vision-based inspection of large concrete structures", *Adv. Struct. Eng.*, **17**(3), 303-318. https://doi.org/10.1260/1369-4332.17.3.303

Kim, H.J., Ahn, E.J., Cho, S.J., Shin, M.S. and Sim, S.H. (2017), "Comparative analysis of image binarization methods for crack identification in concrete structures", *Cement Concrete Res.*, **99**, 53-61.

Kim, J., Kim, S., Park, J. and Nam, J. (2015), "Development of crack detection system with unmanned aerial vehicles and digital image processing", *Proceedings of the Advances in Structural Engineering and Mechanics (ASEM15)*, Incheon, Korea, August.

Kanatani, K., Ohta, N. and Kanazawa, Y. (2000), "Optimal homography computation with a reliability measure", *IEICE T. Inform. Syst.*, **83**(7), 13691374.

Lee, F.W., Chai, H.K. and Lim, K.S. (2017), "Characterizing concrete surface notch using Rayleigh wave phase velocity and wavelet parametric analyses", *Constr. Build. Mater.*, **136**, 627-642. https://doi.org/10.1016/j.conbuildmat.2016.08.145

Liu, Y., Cho, S., Spencer, B.F. and Fan, J. (2014), "Automated assessment of cracks on concrete surfaces using adaptive digital image processing", *Smart Struct. Syst.*, **14**(4), 719-741. http://dx.doi.org/10.12989/sss.2014.14.4.719

Sham, F. C., Chen, N. and Long, L. (2008), "Surface crack detection by flash thermography on concrete surface", *Insight: Non-Destructive Testing and Condition Monitoring*, **50**(5), 240-243. https://doi.org/10.1784/insi.2008.50.5.240

Tawie, R., Lee, H.K. and Park, S.H. (2010), "Non-destructive evaluation of concrete quality using PZT transducers" *Smart Struct. Syst.*, **6**(7), 851-866. http://dx.doi.org/10.12989/sss.2010.6.7.851

Vidas, S., Lakemond, R., Denman, S., Fookes, C., Sridharan, S. and Wark, T. (2012), "A mask-based approach for the geometric calibration of thermal-infrared cameras", *IEEE T. Instrum. Measurement*, **61**(6), 1625-1635. https://doi.org/10.1109/TIM.2012.2182851

Yang, J.Y., Hwang, S.K., An, Y.K., Lee, K.H. and Sohn, H. (2016), "Multi-spot laser lock-in thermography for real-time imaging of cracks in semiconductor chips during a manufacturing process", *J. Mater. Process. Tech.*, **229**, 94-101.

Zhang, Z. (2010), "A flexible new technique for camera calibration", *IEEE T. Pattern Anal. Mach. Intell.*, **22**(11), 1330-1334.

Zhang, Y., Larose, E., Moreau, L. and D'Ozouville, G. (2017), "Three-dimensional in-situ imaging of cracks in concrete using diffuse ultrasound", *Struct. Health Monit.*, **I-6**, 1-9. https://doi.org/10.1016/j.aqpro.2013.07.003

Zenzinger, G., Bamberg, J., Satzger, W. and Carl, V. (2007), "Thermographic crack detection by eddy current excitation", *Nondestruct. Test. Eval.*, **22**(2-3), 101-111. https://doi.org/10.1080/10589750701447920